Induction Motors versus Permanent Magnet Actuators for Aerospace Applications

Panagiotis E. Kakosimos, Athanasios G. Sarigiannidis, Minos E. Beniakar, Antonios G. Kladas and Chris Gerada

Abstract—This paper introduces a comparative study on the design of aerospace actuators concerning Induction Motor (IM) and Permanent Magnet Motor (PMM) technologies. In the analysis undertaken, the two candidate configurations are evaluated in terms of both their electromagnetic and thermal behavior in a combined manner. On a first step, the basic dimensioning of the actuators and their fundamental operational characteristics are determined via a time-stepping Finite Element (FE) analysis. The consideration of the thermal robustness of the proposed motor configurations is integrated in the design procedure, through the appropriate handling of their respective constraints. As a result, all comparisons are carried out on a common thermal evacuation basis. On a second step, a single objective optimization procedure is employed, considering several performance and efficiency indexes using appropriate weights. Manufacturing and construction related costs for both investigated topologies are considered employing specific penalty functions. The impact of the utilized materials is also examined. The resultant motor designs have been validated through manufactured prototypes illustrating their suitability for aerospace actuation.

Index Terms—Actuators, aerospace engineering, finite element methods (FEM), induction motors (IMs), machine design, geometry optimization, permanent magnet motors (PMMs).

NOMENCLATURE

v : magnetic reluctivity
A : magnetic vector potential
J_S : source current density
σ : electrical conductivity
V : electric potential
H_C : coercive force of the permanent magnet
R : phase resistance
L : end windings inductance
i_s : stator current
v_s : supply voltage
l : active motor length
n_c : number of conductors
S : total conductor surface
S^+ : total surface of conductors with positive phase current
S^- : total surface of conductors with negative phase current
F_t : tangential component of the magnetic force
P_t : mean tangential pressure
S_g : air-gap surface
T : electromagnetic torque
R_r : rotor radius
B_n : normal magnetic flux density component
B_t : tangential magnetic flux density component
θ : angular coordinate
σ_m : radial magnetic force density
X_k : design variables vector
L_{tooth} : length of stator teeth
W_{t1} : width of stator teeth
W_{t2} : width of stator tooth tip
X_0 : vector of initial values of the design variables
$G_{1,..,5}$: weight coefficients
T_m : mean electromagnetic torque
T_r : electromagnetic torque ripple
A_n : 3rd and 5th normalized amplitude sum
P_c : copper losses
g : problem constraints
C_1 : term associated with the winding fill factor
C_2 : term associated with the slot shape
C : total technical cost
k : ratio of end-ring resistance to bar resistance
θ_m : mechanical angle
V_{DC} : DC bus voltage
I_{abc} : measured three phase line currents
v_q^* : q-axis reference voltage
v_d^* : d-axis reference voltage
V_{abc}^* : three phase reference voltages

P. E. Kakosimos, A. G. Sarigiannidis, M. E. Beniakar and A. G. Kladas are with the Department of Electrical and Computer Engineering, Laboratory of Electrical Machines and Power Electronics, National Technical University of Athens, 9 Iroon Polytechneiou street, 15780 Zografou Athens, Greece (email: panoskak@gmail.com).

C. Gerada is with the Department of Electrical and Electronic Engineering, The University of Nottingham, NG7 2RD Nottingham, U.K.

I. INTRODUCTION

THE latest general direction in the industry of electric motors is biased towards the better utilization of rare-earth materials. This tendency is focused on two main alternative strategies, i.e. the complete substitution of existing

and entrenched technologies or their adaptation to the new topology trends through their systematic refinement emphasizing on their operating efficiency increase. That technological transition combined with the current advances in permanent magnet technologies, renders the extensive use of rare-earth magnets feasible, even under severe thermal environmental conditions [1]. Permanent Magnet Motors (PMMs) and PM assisted motors exhibit numerous advantages and constitute an attractive solution for almost every particular application. However, a clear indication towards the potential limitation on the usage of Induction Motors (IMs) and their eventual replacement has not yet been established. This is more intensely evident in industrial applications, such as pulp or paper/forest products industry, where IMs are traditionally the dominant technology [2]. On the contrary, in aerospace actuation applications an increasing tendency towards the integration of PMM topologies is apparent; boosting their domination rates. This is basically attributed to the fact that they satisfy the spatial limitations and constraints, dictated by the strict nature of such applications. Nevertheless, the choice of the more advantageous between the two candidate motor configurations is application specific, as they both benefit from their particular operating characteristics [2–4].

More specifically, PMMs feature crucial inherent advantages over the alternative motor topologies [5], [6]. Consequently, they have attracted a rapidly growing interest within the scientific community [7], especially for high power density actuation applications highlighting the necessity for their thorough investigation [8]. In aerospace applications, along with the demand for high performance, safety and reliability issues arise. The extremely strict nature of the specifications, both operational and spatial, dictate the necessity for further investigation of their operation [9], [10]. The most important advantages of PMMs lay on the fact that the PMs constitute an independent and strong excitation system. This feature enables substantial overloading of the motor while providing higher torque density values. The fact that no electromagnetic excitation system is employed additionally enhances their transient behavior, while simplification and maintenance are also two significant beneficial factors. The abovementioned advantages have led PM motors to be considered a viable and attractive solution [4], [11–12]. On the other hand, their main disadvantages concern their operation under fault conditions. Their serious thermal constraints under fault conditions, their limited fault tolerance capabilities, the PMs retention and demagnetization issues and the need for high braking torque, are major bottlenecks against their widespread usage. [13].

The predominant motor technology in such applications for many years has been the cage IMs. Their superior dynamic behavior in conjunction with their brushless nature, that enables their operation without the presence of commutator or slip rings, renders them suitable for high performance controlled operation in electric drive applications [14–16]. The dramatic advance in the area of power electronics and automatic control technologies has significantly contributed to

their establishment as standard motors in electrical drives, when field weakening operation in high speeds is required. However, the IMs technology exhibits numerous disadvantages as well, both constructional and operational. For example, their relatively small air gap length and their inferiority against the synchronous motors in terms of overall efficiency and power factor are major drawbacks. Great scientific effort has been made over the past years in order to limit the impact of the aforementioned disadvantages. Advancements in the area of motor design and motor drives have facilitated cost efficient motor operation over a wide speed range without compromising their efficiency and reliability.

In this paper, the design process and the comparison in terms of operational characteristics of two motor topologies, a PMM and an IM, satisfying the specifications of a specific aerospace application, is presented. Two distinct and extremely different operating conditions are considered for both motor topologies accounting also for emergency operation. In order to determine the fundamental actuator operating characteristics and the precise stator and rotor geometries, FE models are employed, integrated in an advanced optimization routine. The severe environmental conditions in aerospace applications are also taken into consideration during the design process. As the impact of the ambient temperature rise is of paramount importance, extensive thermal analysis has been conducted in order to satisfy the equal thermal evacuation basis criterion for each configuration. The two candidate actuator configurations are illustrated in Fig. 1. On a next step, manufacturing and materials utilization related issues are further investigated. The analysis is mainly focused on the formation of the end-rings mostly concerning the IM topology. The implemented design methodology has been validated through the manufacturing and experimental testing of two prototypes, a PMM and an IM respectively, while for the case of the IM, two different end-rings formations have been tested.
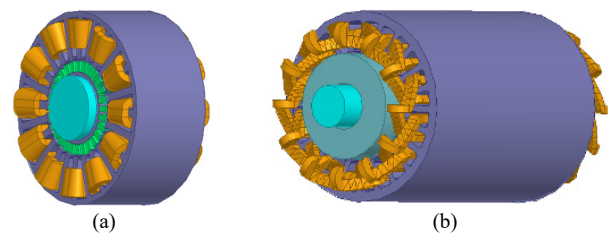

Fig. 1. 3D actuator representation models.
(a) 24 slots - 28 pole PM machine. (b) 8 pole induction machine.

II. ACTUATOR SPECIFICATIONS

Certain geometrical and electromechanical specifications, dictated by the application nature, have to be satisfied by the actuator geometry. The main actuator specifications and dimensions are tabulated in Table I, for the two different operation modes. The actuator output torque capability under normal operation is about five times less compared to the extreme mode of operation. A respective increase in rotor speed is also evident. Such a duality in the motor

specifications is quite typical in aerospace applications. This is mainly attributed to safety reasons, to prevent undesirable effects of disturbances on the actuator operation during certain maneuvers. It is worth pointing out that the speed value, as shown in Table I, is the actual machine mechanical speed without the usage of step down gear. The main restrictions are now set by the control system capacity, dc voltage level and switching frequency.

Quantity		Value
Normal operation	Torque, Nm	1.2
	Speed, rpm	180
Extreme operation	Torque, Nm	6.0
	Speed, rpm	6000
DC link voltage, V		270
Maximum outer diameter, mm		90
Maximum length, mm		120

In the process of determining the basic motor dimensions, a preliminary analysis, based on analytical formulas, has been carried out for the two actuator types. For the needs of the analysis the fundamental design principles have been initially considered. However, each machine type required special attention during the design procedure regarding the satisfaction of the listed requirements and both the respective geometrical and spatial limitations.

III. MODELING AND DESIGN CONSIDERATIONS

The time-dependent magnetic field is governed by the well known Maxwell's equation in the form of the magnetic vector potential:

$$\nabla \times v \nabla \times A = J_s - \sigma \frac{dA}{dt} - \sigma \nabla V + \nabla \times H_c \tag{1}$$

The equation describing the interaction of the magnetic field with the applied machine terminal voltage is of the following form:

$$v_s = R \cdot i_s + L \cdot \frac{di_s}{dt} + \frac{l \cdot n_c}{S} \cdot \left(\iint_{s^+} \frac{\partial A}{\partial t} dS - \iint_{s^-} \frac{\partial A}{\partial t} dS \right) \tag{2}$$

On a first step, in order to specify the main motor design characteristics, a preliminary design analysis has been implemented. Particularly, for the IM, conventional design principles have been followed, mainly focusing on the efficiency and the output torque. The produced electromagnetic torque can be calculated from the mean tangential pressure of the magnetic forces on the gap of the machine, which is expressed by means of Maxwell stress tensor as follows:

$$F_t = P_t \cdot S_g \tag{3}$$

$$T = R_r \cdot F \rightarrow T = 2\pi R_r^2 \cdot l \cdot P_t \tag{4}$$

$$P_t = \frac{1}{\mu_0} \oiint B_n \cdot B_t \cdot dc \tag{5}$$

Different topologies and winding configurations suitable for the specific application have been investigated and compared, in order to identify the one exhibiting the best performance with respect to the considered specifications. The non-overlapping winding investigation has shown that under such circumstances and topology, a non-overlapping winding is not favorable and effective for the IM, thus the classical winding layout has been considered. In order the IM to meet the requirements the whole available space, maximum length and diameter, is required to be covered taking into consideration the best performance. In this case of inverter fed motor, minimization of rotor resistance is desirable. This constraint has been considered at the design stage of the proposed motor configuration. Finally, a sensitivity analysis of the main motor parameters of the selected configuration has been performed in order to define the detailed motor design shown in Fig. 1.

Contrary to the IM case, as far as the PMM is concerned, a systematized analysis of the most popular alternative motor geometries and of the most suitable winding configurations, for this specific application, has been undertaken. The analysis was mainly focused on the key points of performance, efficiency and reliability. The active machine length for the case of the PM motor has been finally set to 40 mm, which is one third of the total available length. Moreover, both overlapping and non-overlapping winding configurations have been considered, and their potential suitability has been evaluated. The non-overlapping single layer winding was considered the most favorable option due to its underlying advantages of lower copper losses and lower torque ripple [19]. Owing to the non regularly distributed magnetic forces along the air-gap, a unidirectional pulling force that rotates with time and generates noise and vibration in the motor is present under such winding configurations [19]. Radial magnetic forces are computed by Maxwell stress tensor as follows:

$$\sigma_m(\theta,t) = \frac{1}{2\mu_o} \cdot \left(B_n^2(\theta,t) - B_t^2(\theta,t) \right) \tag{6}$$

By the end of the preliminary design process, and the selection of the final winding layout, a particular evolutionary optimization algorithm has been employed. The algorithm facilitated the comparative approach on the stator geometry optimization of surface PM machines involving fractional slot concentrated winding configurations, considering the variation of key stator design variables. More specifically, a zero order-direct search Rosenbrock based optimization algorithm is introduced in order to minimize an application-specific penalty function through a Sequential Unconstrained Minimization Technique (SUMT) [17]. Fig. 2 illustrates the block diagram of the proposed optimization procedure. The procedure is based on the interaction between a 2-D FEM parametric model and the optimizer block.

The penalty function at the beginning of k_{th}-iteration shown in the block scheme is given in [18]:

$$P^k(\boldsymbol{X_k}) = G_1 \cdot \frac{T_m(\boldsymbol{X_k})}{T_m(\boldsymbol{X_0})} + G_2 \cdot \frac{T_r(\boldsymbol{X_k})}{T_r(\boldsymbol{X_0})} + G_3 \cdot A_n(\boldsymbol{X_k})$$

$$+ G_4 \cdot \frac{T_m(\boldsymbol{X_k})}{\sqrt{P_{Cu}(\boldsymbol{X_k})}} \cdot \left(\frac{T_m(\boldsymbol{X_0})}{\sqrt{P_{Cu}(\boldsymbol{X_0})}} \right)^{-1} + G_5 \cdot \frac{C(\boldsymbol{X_k})}{C(\boldsymbol{X_0})} \qquad (7)$$

$$+ R^k \cdot \sum 1/(g_i(\boldsymbol{X_k}))$$

where $\boldsymbol{X_k}$ is equal to $[L^k_{tooth}, W^k_{t1}, W^k_{t2}]$ and $g_i(\boldsymbol{X_k}) \geq 0$, $i = 1,2,3$. The total technical cost C is expressed as:

$$C^k(\boldsymbol{X_k}) = C_1 \cdot \max\left(\frac{L^k_{tooth}}{L}, \frac{W^k_{t2}}{W} \right) + C_2 \cdot \max\left(\frac{W^k_{t1}}{W^k_{t2}}, \frac{W^k_{t2}}{L^k_{tooth}} \right)$$

$$= \sum_{i=1}^{4} \sum_{j=1}^{3} a_{ij} \exp\left(-\left((x_i - b_{ij}) \middle/ c_{ij} \right)^2 \right) \qquad (8)$$
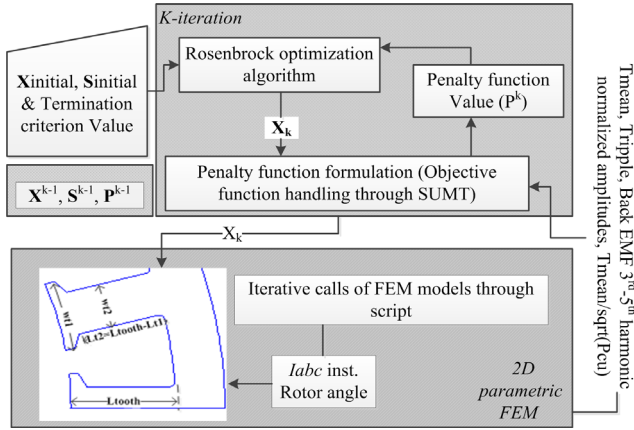

Fig. 2. Block scheme of the adopted optimization algorithm [22].

IV. INDUCTION MOTOR ACTUATOR CASE

The absence of excitation on the rotor of induction motors is its most important characteristic regarding the establishment of the rotor magnetic field. To achieve adequate torque production, it demands higher current density to flow into the stator. As a result, it is reasonable that under these circumstances the IM requires larger envelope dimensions than a PM machine in order to achieve the equal output torque under the same stator current density levels. In Fig. 3 the output torque versus slip frequency is illustrated for different stator current densities and active motor lengths. For all cases an actual slot fill factor equal to 0.5 and constant currents have been considered.

From Fig. 3 it can be derived that the eight-pole IM configuration meets the prescribed specification values at the maximum available machine length of 120 mm. It should be noted that a thermally acceptable current for the normal operating conditions is of about 6 A/mm². Power factor under normal and extreme operating condition versus speed is illustrated in Fig. 4. The motor nominal operating conditions according to the design procedure involve low speed operating range shown in Fig. 4a presenting appropriate power factor values. In counterparts the low power factor encountered in high speed ranges corresponding to extreme operating conditions are not compromising the overall actuator behavior as such conditions are rarely implemented in case of emergencies.

Fig. 5 shows the power loss density distribution for the IM, considering both modes of operation. The actual supplied current density is 6 A/mm² and 13 A/mm², respectively. For the specific current density values, the required torque levels are achieved and the stator and rotor core materials are optimally utilized, i.e. they operate at the knee of the laminations BH curve, which is a design process criterion. The preservation of saturation at low levels leads to increased sinusoidality of the back EMF waveform. Fig. 6 illustrates the unsaturated core for the normal operation. For this case, the EMF is almost sinusoidal. The EMF for the extreme operating conditions exhibits insignificant signs of harmonic distortion, also indicating the operation at the knee of the magnetizing curve.
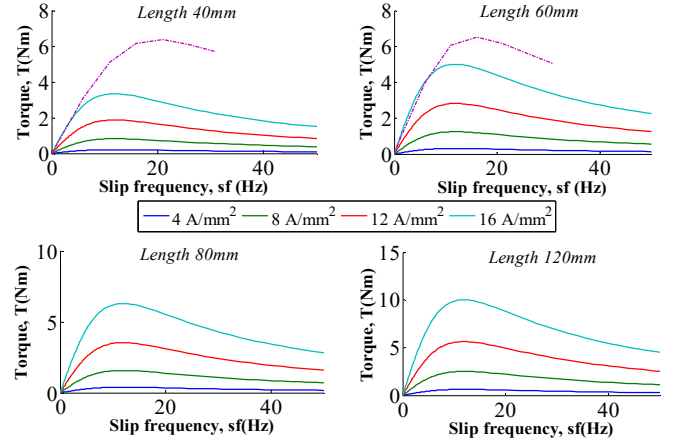

Fig. 3. Torque profile versus slip frequency considering constant stator current densities. The dotted line corresponds to 28 and 20 A/mm² for machine lengths equal to 40 and 60 mm, respectively.
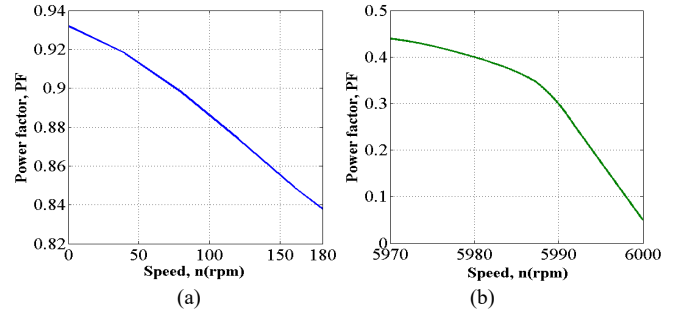

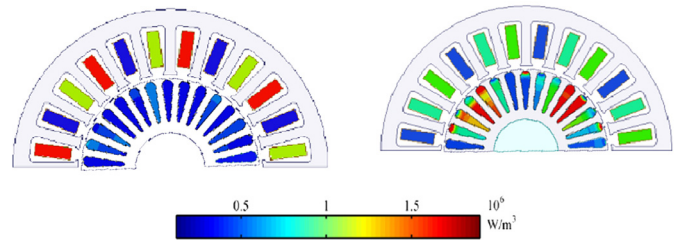Fig. 4. Power factor versus speed under (a) normal and (b) extreme operating conditions.

Fig. 5. Power loss density distribution under normal (left) and extreme (right) operating conditions.

The reduction of parasitic torque, additional losses, noise and vibration is crucial for the selection of the stator and rotor number of slots. However, the construction of multi-pole and of small size machines significantly reduces the available and feasible stator and rotor slots combinations. To evaluate the

most appropriate combination between the stator and rotor numbers of slots several possible combinations have been investigated. Due to manufacturing limitations 24 stator slots were considered. The cross sections of the copper bars and the rotor bore have been kept constant in order not to compromise the comparability of the results under the equal output torque. Table II presents the torque ripple under normal operation of five distinctive cases that were examined and indicates the impact of the increase of the number of rotor slots on produced torque.
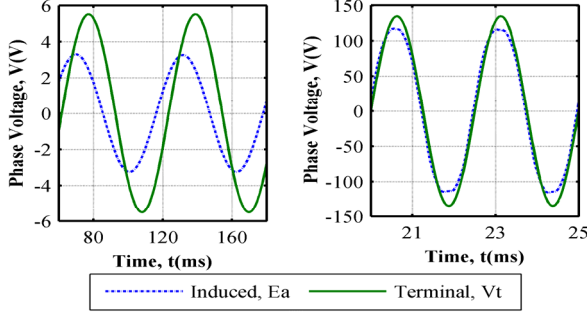

Fig. 6. Induced and terminal phase voltage under normal (left) and extreme (right) operating conditions.

TABLE III
ROTOR SLOTS CHARACTERISTICS

Number of rotor slots	Torque ripple (Nm)
26	3.02
30	1.98
35	0.67
38	1.67
58	1.83

When the number of the rotor slots increases significantly, the rotor teeth are heavily saturated, resulting in an increase in the torque ripple. Furthermore, due to the limited available space, a compromise between manufacturing feasibility and the theoretical optimum approach should be made. From Table II it is evident that the 30 slots in rotor benefit from the increased slot number constituting also an adequately satisfactory version. Another important factor that has to mandatorily be taken into account is the rotor moment of inertia, as it directly improves the motor dynamic performance. The existence of the copper in the rotor slots deteriorates the machine behavior during speed variations. The IM rotor involves a moment of inertia slightly lower than $5 \cdot 10^{-4}$ kg.m^2.

An important issue in achieving high efficiency in the IM design case concerns low rotor resistance enabled through arc copper welding formation of cage end-rings. However, in the reduced rotor geometries favored in aerospace applications it is difficult to implement such manufacturing procedures resulting in usual end-ring resistance values of the order of 25% of rotor resistance. That is why silver joint end-ring formation has to be considered involving rather greater end ring resistance values [14]. The use of die-cast rotor cage could reduce the high end-ring resistance values; however it is quite demanding to be implemented in such space-limited applications. In order to take into account this constraint, variation of end-ring resistance impact on the motor

performance has been investigated at the design stage. The respective torque-speed characteristics for ideal end-ring hypothesis (zero resistance) and different end ring resistance values have been investigated at the design stage and shown in Fig. 7. This figure illustrates the importance of achieving low end-ring resistance values [18]. The term k represents the ratio of end-ring resistance to bar resistance. For the arc copper welding and silver joint end ring formations an actual ratio of about $k_1 = 1.5$ and $k_2 = 2.5$ has been considered, respectively.
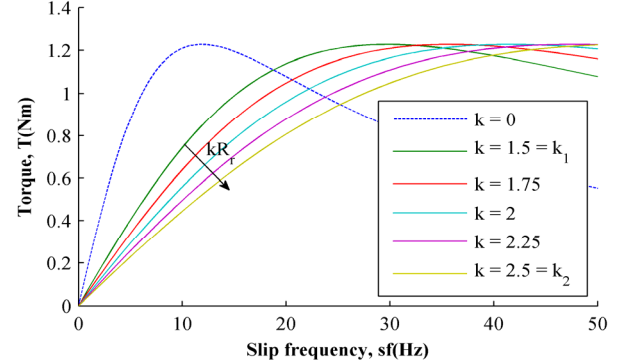

Fig. 7. Torque versus slip frequency for different estimated rotor resistances.

V. PM ACTUATOR CASE

Regarding the winding configuration for the PM actuator, the non-overlapping single layer winding was adopted, as concentrates the most benefits of the investigated winding topologies. Even though the alternate teeth wound winding is considered a more favorable choice, it presents some serious drawbacks. The number of poles and slots has to be chosen with extreme care, in order to maintain high values for the winding factor and minimize the values of the torque ripple and the rotor losses respectively, which incur a significant increase in machine noise [19]. In order to indentify the favorable winding layout and the numbers of rotor poles and stator slots, different winding topologies have been examined by using the time-stepping FE analysis in conjunction with the optimization procedure.

Table III summarizes the main characteristics of some of the analyzed winding layouts, while considering identical embrace and thickness of the magnet configuration under the same voltage supply.

TABLE III
WINDING LAYOUT CHARACTERISTICS

	Winding layout	Rotor poles	Torque ripple (%)	Winding factor
Single a.	B|A|A′|C′|C|B…	20	2.24	0.966
Single g.	B|A|A′|A|A′|C′|C|C′|C|B…	22	1.55	0.958
Single c.	B|A|A′|A|A′|C′|C|C′|C|B…	26	1.39	0.958
Single e.	B|A|A′|C′|C|B…	28	1.28	0.966
Double b.	B′A|A′A′|AC′|CC|C′B…	20	1.72	0.933
Double d.	B′A|A′A′|AA|A′A′|AC′|CC…	26	1.06	0.950
Double f.	B′A|A′A′|AC′|CC|C′B…	28	0.91	0.933
Double h.	B′A|A′C|C′B…	32	4.16	0.866

The MMF harmonic component in PM machines with fewer stator slots than rotor poles that contributes in the mean torque production is not the fundamental but a higher harmonic component of the same order as the number of pole

pairs. The 24 stator slots and 28 rotor poles single layer fractional slot machine configuration has been selected for this particular application and specifications exhibiting low torque ripple with high winding factor, and subsequently, higher EMF capacity.

The radial force density distribution for the selected topology under nominal operating conditions, calculated by (6) versus the rotor angle in the air-gap is illustrated in Fig. 8. It may be noted that the resulting radial magnetic force per one rotating period is negligible and approaches 0.47 N. Such a low total radial force is a result of the symmetry of the applied winding layout. Fig. 9 shows the power loss density distribution of the PM under both operations considered.
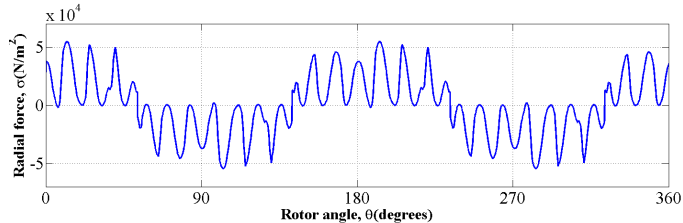
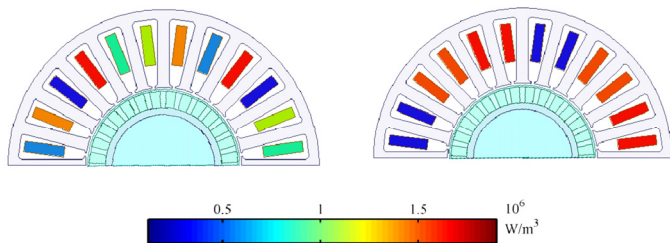Fig. 8. Radial force density distribution for a rotating period.

Fig. 9. Power loss density distribution under normal (left) and extreme (right) operating conditions.

The capability of the motor to operate under overloading conditions is of high importance; enabling to meet the requirements of the extreme loading condition. The torque angle, under normal operation, is approximately equal to 30 degrees and the EMF is absolutely sinusoidal, which is mainly due to the unsaturated stator and rotor core materials. Fig. 10 depicts the induced and terminal phase voltage considering a sinusoidal voltage supply at the machine terminals. Under the extreme operating condition, the maximum torque at maximum speed is significantly higher than the specified torque for the normal operation.
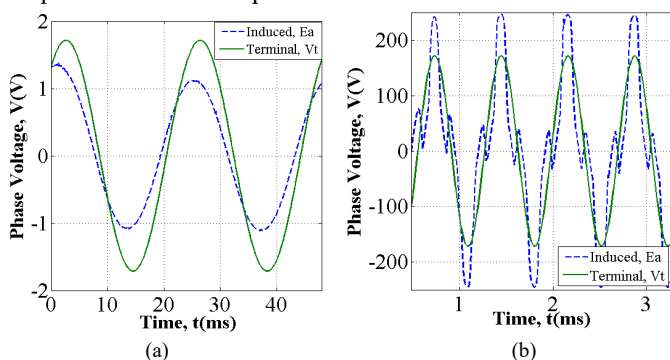

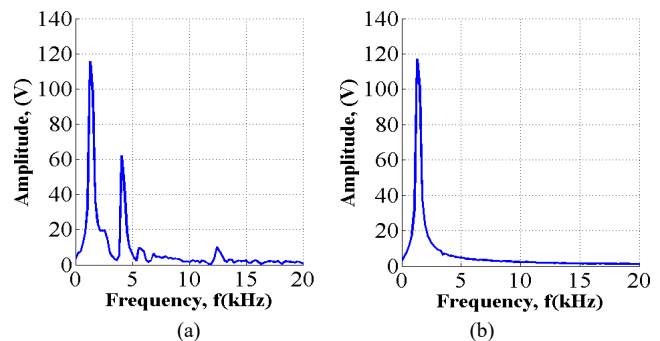Fig. 10. Induced and terminal phase voltage under normal (a) and extreme (b) conditions.

Fig. 11. Fourier analysis of the induced (a) and terminal phase voltage (b).

The stator and rotor laminations are driven to high saturation levels presenting mean flux density in the stator tooth equal to 2 T. Subsequently, the induced EMF is affected by the highly saturated laminations presenting a 3rd harmonic component equal to the 50.8% of the fundamental component. The induced EMF and terminal voltage as well as the harmonic content are illustrated in Fig. 10 and Fig. 11, respectively. In high speed operating conditions PMM topologies are expected to present reduced field weakening capability [20]. The action of field weakening procedure is to lower the influence of the PMs flux linkage on the resulting air-gap flux, thus it is obvious that this constitutes a PMMs drawback especially when compared to IMs which feature the absence of excitation. In this specific application, the highest speed foreseen is the nominal one, however the possibility of field weakening for inverter protection under small overspeed, which could be encountered due to mechanical load abrupt variation, is desirable.

VI. RESULTS AND DISCUSSION

IM drawbacks derive primarily from the absence of independent electromagnetic excitation in the rotor. As it has already been mentioned, higher current density in the stator is needed in order to obtain equal output torque levels due to the establishment of the rotor magnetic field. Therefore, overall IM situation deteriorates compared to the PM machine.
From the preceded analysis, IM required the total available length, while the PM actuator demanded the one third of the total length, in order to satisfy the specifications. However, PM machine, under the extreme operating condition, presents stator and rotor core heavy saturation in order to achieve the desirable output torque, resulting in distorted induced EMF and currents. Unlike the PM machine, the IM core saturation level is lower, due to the fact that the magnetic field in the rotor has already been established, thus having the capability of being further loaded. It should be noted that geometry optimization has been carried out for the normal operation for the two motor types. For the normal operation, the main PM and IM characteristics are tabulated in Table IV. It is worth mentioning that the applied current density of about 4 A/mm^2 is too low for aerospace actuators. In practice, a forced air or oil cooling is used and the current density is higher. However, the extreme mode operation necessitates higher current densities setting the operation limits and leading to lower

densities under normal operation. Nevertheless, in the present study natural air convection has been considered.

TABLE IV
PM AND INDUCTION ACTUATOR CHARACTERISTICS

Quantity	PMM	IM
Current density, J (A/mm^2)	4.14	4.05
Depth, l (mm)	40	120
Number of conductors	47	11
Number of branches	4	1
Volume, V (m^3)	1.14e-4	4.55e-4
Torque density, (kNm/m^3)	10.5	2.42
Stator slots	24	24
Rotor slots	-	30
Poles	28	8

Moreover, in aerospace actuation applications, the operation of more than one machine on the same shaft is very common practice, mainly for safety and reliability reasons, thus contributing to a fault tolerant system. As a result, when a machine fault occurs, the remaining machines have to operate overloaded in order to substitute the fault machine operation and not to be interrupted. The absence of rotor excitation favors the IMs, which exhibit zero braking torque under short circuit fault. Fig. 12 indicates the main disadvantage of the PMMs, which accounts for their thermal constraints under fault conditions. When a three phase short circuit is imposed at 20 ms, the PM machine continues to contribute with high braking torque equal to 0.5 Nm after 40 ms, while, on the contrast, the IM presents almost zero braking torque.

The final choice of actuator type strongly depends on the specific application demands and particularities. Both candidate actuator types exhibit major differences and corresponding advantages. It should be noted that, for this specific aerospace application, the equal thermal evacuation criterion has been considered and strongly influenced the results. As the extreme environmental conditions in aerospace applications contribute to the temperature rise, taking the thermal constraints into consideration is very important. Furthermore, another important factor that should be mentioned is the fact that the rotor temperature is much more crucial in the PMM than in the IM, due to the inherent retention issues of the PMs. A potential temperature increase incurs a dramatic decrease in the remanent flux density of the PMs, which results in a significant decrease in the air-gap flux density and consequently in the deterioration of the motor's overall performance. Fig. 13 shows the temperature variation during normal operating conditions for the two configurations. In particular, the minimum and maximum temperatures correspond to the rotor and the stator respectively. The higher stator temperature values are caused by the fact that it bears the main burden due to the winding establishment. Maintaining approximately equal heat flux levels for each configuration, the PMM topology seems to be favored as it involves an important reduction in size and weight with the same thermal constraints.
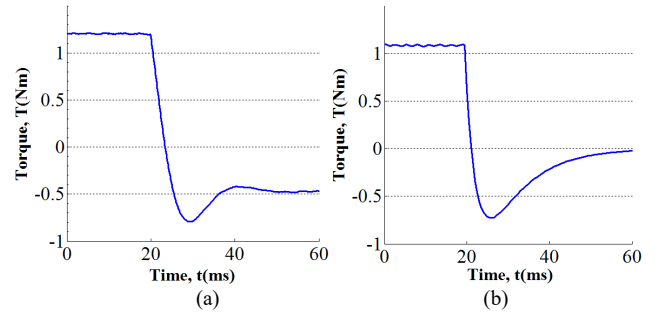

Fig. 12. Instantaneous torque under three phase short circuit fault considering constant speed load. (a) PM machine. (b) IM.
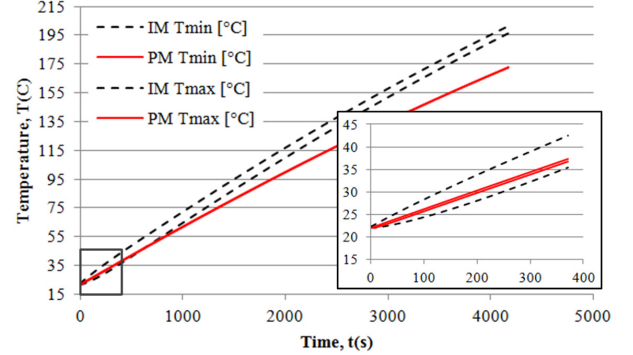

Fig. 13. IM and PMM temperature variation under normal operating conditions.

VII. EXPERIMENTAL VALIDATION

In order to experimentally demonstrate the developed methodology, the experimental setup shown in Fig. 14 has been employed. The experimental setup comprises the control and power unit, and an electromechanical brake so as to apply variable mechanical loads to both prototypes.

The constructed multipurpose control unit receives and processes signals of the voltage and current transducers, and outputs the desirable pulses. Fig. 15 shows signal routing from and to the main component of Digital Signal Processor (DSP). The employed DSP presents an adequate computational capability for this specific application supplying the IM and PMM prototypes with an SPWM voltage employing a carrier frequency of 10 kHz. In order to capture the presented data in the following section, a TiePie oscilloscope and a National Instrument PXI (16bit, 4MS/s) are used.
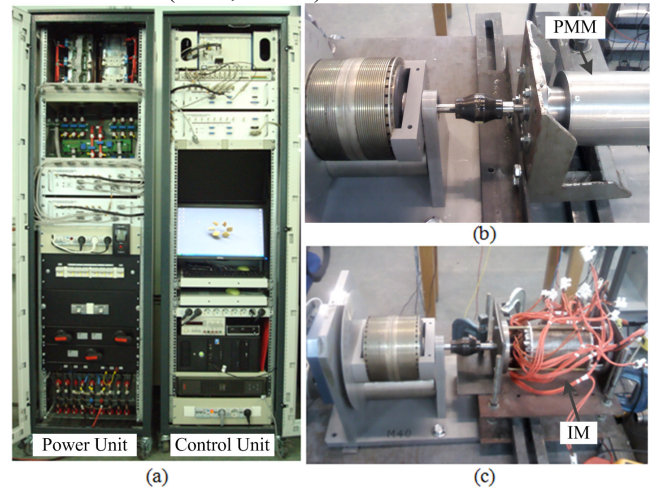

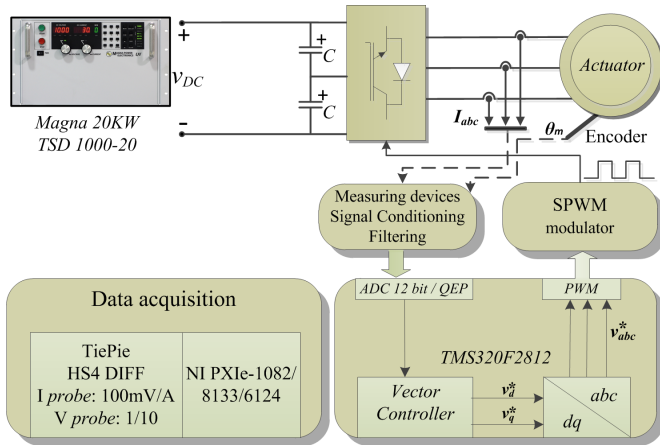Fig. 14. (a) Power and control unit. (b) PMM (c) IM .

Fig. 15. Overall system configuration.

Fig. 17. Measured phase voltage and current of IM under no load operation at 180 rpm.

Fig. 18. Measured phase voltage and respective harmonic content of IM at 6000rpm.

(a)

(b)

Fig. 19. Measured torque under constant current density as a function of slip frequency for both end ring formations. (a) Arc welding. (b) Silver joint.

Validating the design methodology, a PMM and an IM prototype have been manufactured, while in the case of the IM two different end-rings formations are also investigated. Fig. 16 shows the IM configuration, as well as both manufactured rotor prototypes with end-rings formation either by using arc welding or silver joint. Stator laminations employed to stator is *Thyssen M 330-35 A / 35JN230.* For the PMM Neodymium (Nd)-Iron (Fe)-Boron (B) *NMX41-EH* has been adopted as PM material. Measured phase voltage and current of IM under no load operation at 180 rpm is depicted in Fig. 17. Although under constant voltage supply the magnetizing current does not significantly depend on load; in this case of inverter supply the magnetizing current of IM is low enough under no load condition. Thus the machine presents low power losses associated with the core due to hysteresis and eddy currents.

In addition, the measured voltage and its harmonic content of the IM at the highest speed of 6000 rpm are illustrated in Fig. 18. Fig. 19 evidences the claims discussed in Section IV and the simulation results shown in Fig. 7 during the design process. Despite silver end joint end-ring formation involves greater end-ring resistance values; it is a preferable choice in cases where machine dimensioning is defined by strict space limitations. Torque versus slip frequency waveforms for both rotor configurations are within the bounds set during design phase, allowing safe selection of materials and manufacturing process to be followed. It should be noted here that the upper and lower bound correspond to the case where the simulated end-ring resistance is comparable to bar resistance (k =1.5) and to greater values (k >1). Significant variations in produced torque for different end-ring formations and speeds are observed in Fig. 19 even in lower slip frequency values, when the motor is inverter driven.
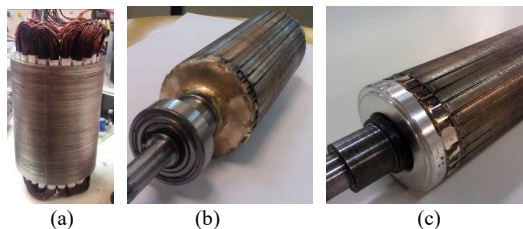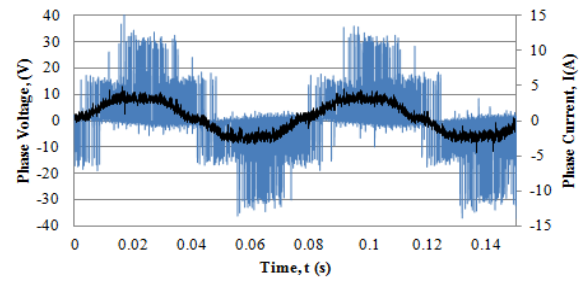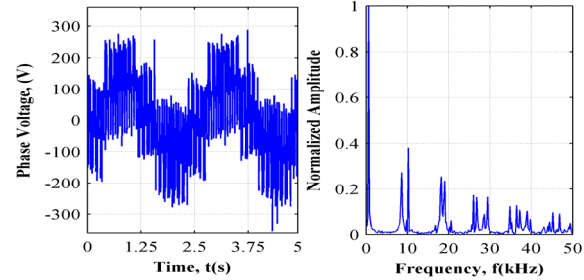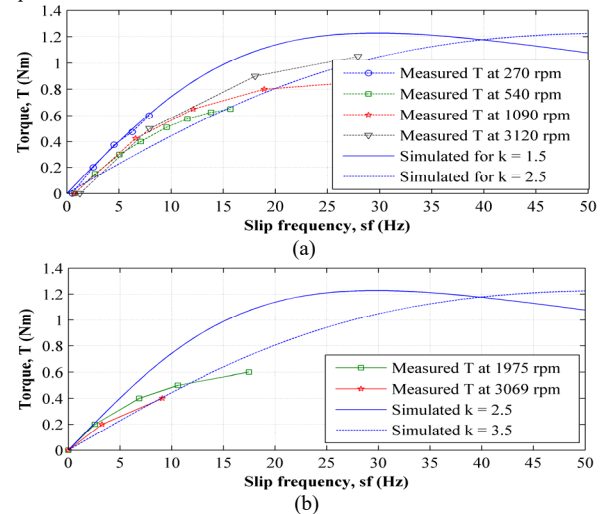

(a)   (b)   (c)

Fig. 16. (a) IM stator. End rings formation by using (b) arc welding or (c) silver joint.

Fig. 20 shows the stator and rotor of the PMM configuration. It is worth noticing here that the magnet retention issue is faced by employing glass fiber support of PMs. Behaving satisfactorily even under 6000 rpm the voltage at the machine terminals presents linear behavior as illustrated in Fig. 21 since the machine is quite far from the knee of laminations B-H curve. Contrarily, it is expected according to the simulation results of under 6000 rpm and full load condition the machine laminations to be under heavy saturation. Simulated and measured torque-speed characteristic for the PMM are shown in Fig. 22, where the simulated results are in good agreement with the measured ones, especially in lower speed range. Measured phase voltage and current of PMM under no load operation at 180 rpm is depicted in Fig. 23, where the current is significantly higher than that of the IM.

Furthermore, the measured voltage and its harmonic content of the PMM at the highest speed of 6000rpm are presented in

Fig. 24. As previously mentioned, for the Sinusoidal Pulse Width Modulation (SPWM) technique implemented by the inverter in PMM and IM, a carrier frequency equal to 10 kHz is utilized. The maximum fundamental electric frequency at the highest speed of 6000 rpm for the PMM is 1.4 kHz, while for the IM is 400 Hz. Therefore, the selected carrier frequency of the SPWM is appropriate to drive both motors adequately for both operating conditions, introducing low harmonic content in the stator current, due to filtering action by winding inductance.

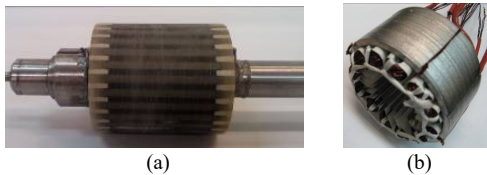(a)   (b)

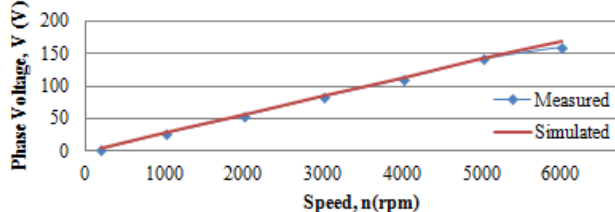Fig. 20. PMM configuration. (a) Rotor. (b) Stator.

Fig. 21. Comparison of measured and simulated phase voltage of PMM under no load operation.
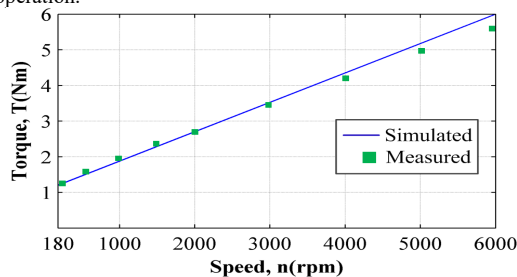

Fig. 22. Comparison of simulated and measured torque-speed characteristic.
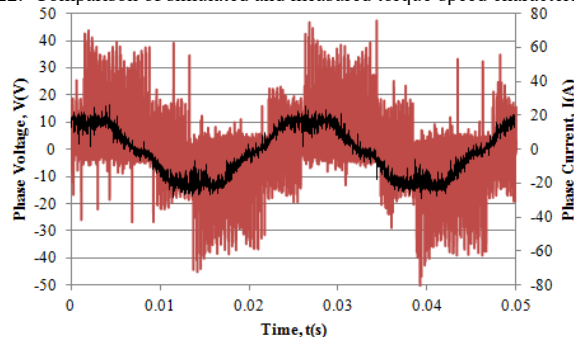

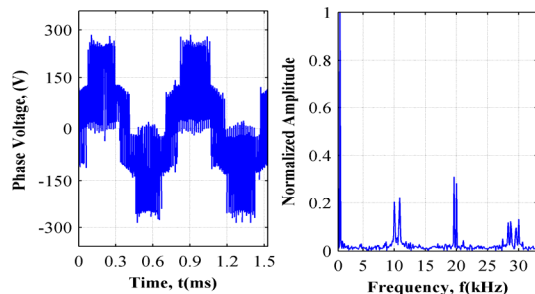Fig. 23. Measured phase voltage and current of PMM under no load operation at 180 rpm.

Fig. 24. Measured phase voltage and respective harmonic content of PMM at 6000 rpm.

VIII. CONCLUSIONS

In this paper a comparative analysis between PMM and IM aerospace actuators has been carried out. Different combinations of rotor-stator slots for the IM and different winding layouts for the PMM have been modeled, and performances are compared. The optimal IM configuration, featured by the absence of rotor magnetic field, required larger dimensioning and weight than the respective PMM one, for the same thermal evacuation ratio. However, the IM case presented lower braking torque and short-circuit currents with respect to the PMM case, leading the final choice of the actuator technology to an overall system considerations dependent problem.

In the considered application the two rival technologies presented different drawbacks: the IM configuration due to the rotor dimensional constraints was difficult to achieve acceptably reduced end ring resistance values compared to bar resistance leading to motor efficiency compromise at low speed ranges. On the other hand the PM configuration, involving surface PM structure, presented increased losses in high speed operating conditions due to reduced field weakening capability. Consequently, through the analysis developed in the paper validated by experimental results, the proposed IM and PMM configurations present complementary advantages, the former concerning fault tolerance characteristics and the later concerning power density issues. Thus, according to the paper findings, on a strict motor basis the PM topology is favored in the considered aerospace application involving two distinct operating speed ranges.

IX. APPENDIX

The losses profile for the *Thyssen M 330-35 A / 35JN230* lamination and the basic characteristics of the *NMX41-EH* PMs are tabulated in Table V.

TABLE V
STATOR LAMINATION LOSSES PROFILE AND PM CHARACTERISTICS

Stator lamination Type: Thyssen M 330-35 A / 35JN230	
Thickness	0.35 mm
Density	7.60 kg/dm^3
Max. Core Losses @ 1.0T, 50Hz	1.30 W/kg
Max. Core Losses @ 1.5T, 50Hz	3.30 W/kg
PM Type: NMX41-EH	
Remanent flux	1.33 T @ 60ºC	1.12 T @ 140ºC
Coercive force	1.52 MA/m @ 60ºC	0.79 MA/m @ 140ºC

REFERENCES

[1] D. G. Dorrell, M.-F. Hsieh, M. Popescu, L. Evans, D. A. Staton, and V. Grout, "A Review of the Design Issues and Techniques for Radial-Flux Brushless Surface and Internal Rare-Earth Permanent-Magnet Motors," IEEE Transactions on *Industrial Electronics*, vol. 58, no. 9, pp. 3741–3757, Sep. 2011.

[2] M. Melfi, S. Evon, and R. McElveen, "Induction versus permanent magnet motors," *IEEE Industry Applications Magazine*, vol. 15, no. 6, pp. 28–35, Nov. 2009.

[3] P. E. Kakosimos, E. M. Tsampouris, A. G. Kladas, and C. Gerada, "Aerospace Actuator Design: a Comparative analysis of Permanent Magnet and Induction Motor configurations," in *20th IEEE International Conference on Electrical Machines*, 2012, pp. 2538 – 2544.

[4] K. I. Laskaris and A. G. Kladas, "Permanent-Magnet Shape Optimization Effects on Synchronous Motor Performance," *IEEE Transactions on Industrial Electronics*, vol. 58, no. 9, pp. 3776–3783, Sep. 2011.

[5] M. Galea, C. Gerada, and T. Hamiti, "Design considerations for an outer rotor, field wound, flux switching machine," in *20th IEEE International Conference on Electrical Machines*, 2012, pp. 171–176.

[6] M.-F. Hsieh and Y.-C. Hsu, "A Generalized Magnetic Circuit Modeling Approach for Design of Surface Permanent-Magnet Machines," *IEEE Transactions on Industrial Electronics*, vol. 59, no. 2, pp. 779–792, 2012.

[7] G. Y. Sizov, D. M. Ionel, and N. A. O. Demerdash, "Modeling and Parametric Design of Permanent-Magnet AC Machines Using Computationally Efficient Finite-Element Analysis," *IEEE Transactions on Industrial Electronics*, vol. 59, no. 6, pp. 2403–2413, 2012.

[8] S. Chaithongsuk, B. Nahid-Mobarakeh, J.-P. Caron, N. Takorabet, and F. Meibody-Tabar, "Optimal Design of Permanent Magnet Motors to Improve Field-Weakening Performances in Variable Speed Drives," *IEEE Transactions on Industrial Electronics*, vol. 59, no. 6, pp. 2484–2494, Jun. 2012.

[9] R. P. Praveen, M. H. Ravichandran, V. T. S. Achari, V. P. J. Raj, G. Madhu, and G. R. Bindu, "A Novel Slotless Halbach-Array Permanent-Magnet Brushless DC Motor for Spacecraft Applications," *IEEE Transactions on Industrial Electronics*, vol. 59, no. 9, pp. 3553–3560, 2012.

[10] M. Villani, M. Tursini, G. Fabri, and L. Castellini, "High Reliability Permanent Magnet Brushless Motor Drive for Aircraft Application," *IEEE Transactions on Industrial Electronics*, vol. 59, no. 5, pp. 2073–2081, 2012.

[11] P. E. Kakosimos and A. G. Kladas, "Modeling of interior permanent magnet machine using combined field-circuit analysis," in *19th IEEE International Conference on Electrical Machines*, 2010, pp. 1–6.

[12] W. Li, H. Qiu, X. Zhang, J. Cao, and R. Yi, "Analyses on Electromagnetic and Temperature Field of Super High Speed Permanent Magnet Generator with Different Material Sleeves," *IEEE Transactions on Industrial Electronics, in Press*.

[13] M. Rottach, C. Gerada, T. Hamiti, and P. W. Wheeler, "A computationally efficient design procedure for actuator motors using magnetic reluctance-and thermal resistance network models," in *20th IEEE International Conference on Electrical Machines*, 2012, pp. 2526–2532.

[14] D. Gerada, A. Mebarki, N. L. Brown, K. J. Bradley, and C. Gerada, "Design Aspects of High-Speed High-Power-Density Laminated-Rotor Induction Machines," *IEEE Transactions on Industrial Electronics*, vol. 58, no. 9, pp. 4039–4047, Sep. 2011.

[15] D. G. Dorrell, A. M. Knight, L. Evans, and M. Popescu, "Analysis and Design Techniques Applied to Hybrid Vehicle Drive Machines: Assessment of Alternative IPM and Induction Motor Topologies," *IEEE Transactions on Industrial Electronics*, vol. 59, no. 10, pp. 3690–3699, 2012.

[16] J. F. Gieras and J. Saari, "Performance Calculation for a High-Speed Solid-Rotor Induction Motor," *IEEE Transactions on Industrial Electronics*, vol. 59, no. 6, pp. 2689–2700, 2012.

[17] E. M. Tsampouris, M. E. Beniakar, and A. G. Kladas, "Geometry Optimization of PMSMs Comparing Full and Fractional Pitch Winding Configurations for Aerospace Actuation Applications," *IEEE Transactions on Magnetics*, vol. 48, no. 2, pp. 943 – 946, 2012.

[18] Y. Gritli, L. Zarri, C. Rossi, F. Filippetti, G. Capolino, and D. Casadei, "Advanced Diagnosis of Electrical Faults in Wound Rotor Induction Machines," *IEEE Transactions on Industrial Electronics*, vol. 60, no. 9, pp. 4012 – 4024, 2013.

[19] J. Krotsch and B. Piepenbreier, "Radial Forces in External Rotor Permanent Magnet Synchronous Motors With Non-Overlapping Windings," *IEEE Transactions on Industrial Electronics*, vol. 59, no. 5, pp. 2267–2276, May 2012.

[20] G. Wang, R. Yang, and D. Xu, "DSP-Based Control of Sensorless IPMSM Drives for Wide-Speed-Range Operation," *IEEE Transactions on Industrial Electronics*, vol. 60, no. 2, pp. 720–727, 2013.

Panagiotis E. Kakosimos (S'12) received the B. Eng. and M. Eng. degree in electrical and computer engineering from the Aristotle University of Thessaloniki, Greece, in 2009 and the Ph.D. degree in 2013 from the Department of Electrical and Computer Engineering at the National Technical University of Athens, Greece.

His current research involves power generation from renewable energy sources, industrial drives, as well as electric machine design optimization for aerospace and electric vehicles applications.

Dr. Kakosimos is a Registered Professional Engineer in Greece.

Athanasios G. Sarigiannidis (S' 13) received the Diploma degree in electrical and computer engineering from the University of Patras, Greece in 2010. He is currently working toward the Ph.D. degree in the Department of Electrical and Computer Engineering, Laboratory of Electrical Machines and Power Electronics, at the National Technical University of Athens, Greece.

His current research involves permanent magnet motor modeling, design and control for traction applications, with emphasis on field weakening techniques for electric motor optimal efficiency control.

Mr. Sarigiannidis is a member of the Technical Chamber of Greece.

Minos E. Beniakar (S'08) received the B. Eng. and M. Eng. degree in electrical and computer engineering from the National Technical University of Athens, Greece, in 2008. He is currently working toward the Ph.D. degree in the Department of Electrical and Computer Engineering, Laboratory of Electrical Machines and Power Electronics, at the National Technical University of Athens, Greece.

His current research involves design optimization of electric motors for aerospace and electric traction applications and industrial drives.

Mr. Beniakar is a Registered Professional Engineer in Greece.

Antonios G. Kladas (SM'10) was born in Greece in 1959. He received the Diploma in Electrical Engineering from the Aristotle University of Thessaloniki, Thessaloniki, Greece, in 1982 and the D.E.A. and Ph.D. degrees from the University of Pierre and Marie Curie (Paris 6), Paris, France, in 1983 and 1987, respectively.

From 1984 to 1989, he was an Associate Assistant with the University of Pierre and Marie Curie. During the period 1991 to 1996, he joined the Public Power Corporation of Greece. Since 1996, he has been with the Department of Electrical and Computer Engineering, National Technical University of Athens, Athens, Greece, where he is currently a Professor. His research interests include transformer and electric machine modeling and design, analysis of generating units by renewable energy sources and industrial drives.

Dr. Kladas is member of the Technical Chamber of Greece.

Chris Gerada (M'05) received the Ph.D. degree in numerical modeling of electrical machines from the University of Nottingham, Nottingham, U.K., in 2005.

Subsequently, he was a Researcher with the University of Nottingham, where he worked on high-performance electrical drives and on the design and modeling of electromagnetic actuators for aerospace applications.

He is currently an Associate Professor in electrical machines with the Power Electronics, Machines and Control Group, Department of Electrical and Electronic Engineering, the University of Nottingham. He is also the Project Manager with GE Aviation Strategic Partnership, Nottingham. His research interests include high-performance electric drives and machines.